Geophysical Journal International

Geophys. J. Int. (2011) doi: 10.1111/j.1365-246X.2011.04944.x

Strain localization and fluid migration from earthquake relocation and seismicity analysis in the western Vosges (France)

Jean-Luc Got,[1] Vadim Monteiller,[1,2] Jocelyn Guilbert,[3] David Marsan,[1] Yves Cansi,[3] Carole Maillard[3] and Jean-Paul Santoire[3]

[1] *ISTerre, Université de Savoie, CNRS, Campus Scientifique,* 73376, *Le Bourget-du-Lac, France. E-mail: jlgot@univ-savoie.fr*
[2] *DTP, Université Paul Sabatier, CNRS,* 14 Av. *E. Belin,* 31400, *Toulouse, France*
[3] *LDG, CEA-DAM Ile-de-France,* BP12, 91680, *Bruyères-le-Châtel, France*

Accepted 2011 January 4. Received 2010 November 23; in original form 2010 June 26

SUMMARY

To understand the mechanisms of intraplate earthquakes, well-documented seismological and geodynamical studies are needed, to provide information for adequate mechanical modelling. This paper describes a detailed analysis of the earthquake sequence associated with the Rambervillers (France) $M \sim 5.4$ earthquake (2003 February 22), which occurred in the western Vosges massif (France), some tens of kilometres to the north of the sites of the Epinal (1973–1974) and Remiremont (1984–1985) earthquake sequences. We computed the location of the mainshock and focal mechanism, together with the double-difference locations of 419 aftershocks of the subsequent earthquake sequence, which included 195 well-recorded similar events (earthquakes with similar waveforms). We combined *pP* phases recorded by remote dense seismic networks with waveform modelling, to accurately determine the mainshock depth (12.5 $\pm$ 1.5 km). Computations of focal mechanisms from regional waveform inversions showed a normal fault plane with a N315° $\pm$ 10° strike and a 45° $\pm$ 15° dip. A detailed space–time analysis allowed two earthquake sequences to be identified: a classic mainshock–aftershock sequence and a secondary sequence that began 250 days after the mainshock. More events were recorded during the secondary sequence than during the main sequence. Very few similar events were recorded during the first 2 days after the mainshock, although data were recorded continuously. Double-difference locations from traveltime differences show that these immediate, non-similar aftershocks occurred in a 4 km $\times$ 2 km subhorizontal area at a depth of about 12 km. Similar events were far more numerous during the secondary earthquake sequence. Double-difference relocation of these similar events revealed a N315° striking, 65° dipping fault plane that is compatible with the mainshock source mechanism. During this later sequence, seismicity oscillated over a vertical range of 2–3 km around a mean depth of approximately 12 km. This observation strongly suggests fluid migration. Normal faulting, subhorizontal faulting and fluid transfer at about 12 km depth can be interpreted in terms of the crust's response (mainshock and post-seismic relaxation) to flexural stresses induced by the alpine compression. This relaxation involves weakening and collapse of the crust, and fluid transfer.

Key words: Earthquake source observations; Seismicity and tectonics; Intra-plate processes.

1 INTRODUCTION

Because intraplate strain localization and earthquake occurrence exhibit varying patterns in limited crustal volumes, they are less well understood than the strain distribution along plate boundaries. As a result, their relation to the regional stress field is not straightforward. Intraplate earthquake swarms may locally exhibit high seismic rates (e.g. Vogtland/Bohemia earthquake swarms, Spicak & Horalek 2001; Fischer & Horalek 2003, 2005) and may include intermediate-to-strong magnitude earthquakes (e.g. New Madrid Seismic Zone, USA, $M \sim 8$, 1811–1812; Charleston, USA, $M \sim 7$, 1886; Tang Shan, China, $M \sim 7.8$, 1976; Ayers Rock, Australia, $M \sim 5.8$, 1989; Bhuj, Gujarat, India, $M \sim 7.5$, 2001). Explanations for such swarms have evoked a variety of mechanisms related to heterogeneities in the stress field or in the strength of the lithosphere (e.g. Sykes 1978; Campbell 1978; Hinze *et al*. 1988; Liu & Zoback 1997; Kenner & Segall 2000; Iio & Kobayashi 2002; Gangopadhyay & Talwani 2003). In most cases, there is little

evidence that can be used to unambiguously constrain the physical mechanism of intraplate earthquakes. This study uses seismological constraints to investigate the occurrence of recurrent intraplate earthquakes and seismic crises in the western Vosges massif (France). This area lies to the west of the Rhine Graben (Fig. 1), a major feature of the European Cenozoic rift system (Ziegler 1992; Prodehl *et al.* 1995). The western Vosges (France) is subject to sporadic seismic activity comprising $M \sim 5$ mainshocks. Since 1962, this activity has been recorded by the LDG-CEA's permanent seismic network. Recent activity (Fig. 1) has been recorded near Epinal (1973–1974), near Remiremont (1984–1985) and, more recently, in the Rambervillers region (2003–present). The western Vosges is thought to have been the source of one of France's most destructive earthquakes, which hit Remiremont in 1682 (intensity VIII MSK, M_l estimated to be 5.3, Lambert 1997). This seismic activity is the expression of tectonic activity in the Vosges–Rhine Graben system. The Rhine Graben is part of the rift system that developed in Central Europe during the Cenozoic. Since the mid-Pliocene, deformation of the Vosges–Rhine Graben area has been driven by left-lateral strike-slip on N–S to NE–SW faults (Abhorner 1975). Recent seismic activity has been in the form of either NE–SW elongated earthquake swarms (Remiremont sequence, 1984–1985, Haessler & Hoang-Trong 1985; Plantet & Cansi 1988) with left-lateral or normal left-lateral strike-slip fault mechanisms, or in the form of NW–SE trending swarms (Epinal, 1973–1974) with right-lateral strike-slip or inverse fault mechanisms. Focal mechanisms in this region have been used to identify a regional stress tensor in which the major and minor principal stresses trend NW–SE and NE–SW, respectively (Delouis *et al*. 1993; Plenefisch & Bonjer 1997). The region is known for its hydrothermal activity, with springs of mineral water of high CO_2 content; three hydrothermal sites are located some tens of kilometres SW of Rambervillers.

The Rambervillers $M_l \sim 5.4$ RéNaSS earthquake (5.9 LDG-CEA—the difference in magnitude estimates is due to different attenuation laws) occurred on 2003 February 22. It is the first $M_l \sim 5$ event to have occurred in this area since the 1682 Remiremont earthquake. It is also one of the largest earthquakes to have occurred in France in the last 50 years. Preliminary results for the mainshock showed a normal strike-slip focal mechanism that is right-lateral on the NW–SE striking, N dipping focal plane (Cara *et al*. 2005).

2 DETAILED SEISMOLOGICAL STUDY OF THE RAMBERVILLERS EARTHQUAKE SEQUENCE

2.1 Mainshock

The Rambervillers $M_l \sim 5.4$ mainshock was recorded by 32 stations of the LDG-CEA permanent seismic network. A routine location for the mainshock (48.33°N, 6.67°E, 10 ± 5 km depth) was computed by inversion of *P*- and *S*-wave first-arrival times. As the first step in this study, we refined the estimation of the mainshock focal mechanism and depth.

Mainshock depth was computed from *pP* phases revealed by cepstral analysis of the waveforms recorded by four remote, dense, short-period seismic arrays located in Mongolia, Nepal, Ivory Coast and Norway. *pP* phases are reflections at the earth's surface of the *P* first-arrival wave train emitted at depth, which is received as a refracted wave at teleseismic distances. In a specific velocity model, the time delay between *P* and *pP* phases strongly constrains the earthquake depth; hence, accurate calculations of earthquake depth require reliable estimates of the *P–pP* time delay. This delay can be obtained through the cepstral analysis of waveforms recorded by a remote seismic array. Cepstrum, which is the Fourier transform of the logarithm of a signal's amplitude spectrum, is one of the tools used to find echoes in a signal.) Cepstrum has been used to detect *pP* phases by Kemerait & Sutton (1982) and Alexander (1996), and Shumway (1971) represented the mean cepstrum to noise cepstrum ratio (the ratio of two χ^2 distributed random variables, which follows a Fisher distribution) and used the F statistic as a detection criterion for the echoes revealed by cepstral analysis. More recently, Bonner *et al*. (2002) applied this approach to the detection of *pP* phases using seismic arrays. They found that filtering the log spectrum around the dominant frequency of the signal strongly increased the reliability of the F statistic to detect *pP* phases. We adopted this approach and filtered the log spectrum between 0.5 and 4.5 Hz. Cepstra were computed for four remote arrays (Mongolia, Nepal, Ivory Coast and Norway) and stacked (Fig. 2a) to highlight the most significant *pP* peaks. We found a *pP–P* time delay of 4.2 ± 0.3 s, which corresponds to a depth of 13 ± 1 km for this earthquake (based on the IASP91 global 1-D velocity model, Kennett & Engdahl 1991).

The mainshock focal mechanism was computed using the inversion of waveforms recorded from five LDG-CEA three-component, long-period seismic stations. The sensors were long-period LP12-type seismometers with a flat transfer function from 0.5 to 300 s. Waveforms were sampled at a 4 Hz sample rate. To allow comparison with synthetic seismograms and inversion, the waveforms were first filtered between 10 and 50 s. Synthetic seismograms were computed in this spectral band using the discrete wavenumber method (Bouchon 1981; Cotton & Coutant 1997). Because local, short-period records of the mainshock provided a ∼2 Hz corner frequency, we chose 0.5 s as the source duration. Propagation was computed using a 1-D velocity model (Table 1). Inversion for determining the optimal source parameters (strike, dip, rake and seismic moment) was performed by minimizing the L1-norm residual variance between the observed and synthetic waveforms, using a grid search and a genetic algorithm. The resulting synthetic waveforms show a good fit with the observations (Fig. 2b). Strike, dip and rake were found to be 316° ± 10°, 44° ± 15° and 108° ± 10°, respectively. The source of the earthquake is therefore a NW–SE normal fault. The computed mainshock seismic moment was 1.7×10^{16} Nm. Finally, we modelled the waveforms recorded at each of the four distant, dense, short-period seismic arrays (Mongolia, Ivory Coast, Nepal and Norway), to check the source parameters (Fig. 2c). The best model was obtained for a depth of 12 ± 1 km.

2.2 Aftershocks

The mainshock was followed by numerous aftershocks, comprising 6 $M_l \sim 3$ earthquakes. About 2000 aftershocks have been recorded (2003–present) by the permanent LDG-CEA seismic network, which consists of 42 stations across France, seven of which are well distributed within an area of between 40 and 120 km around the epicentral zone. Eighty per cent of the aftershocks were recorded by between 4 and 7 stations of the network. For the first 2 months, the aftershock seismicity time distribution approximately followed an Omori law. The aftershock frequency–magnitude distribution shows that the maximal LDG magnitude was 3.7, and the catalogue was complete down to magnitude 1.8. Aftershocks were first located as a dense cluster in a volume of several km^3, centred near 48°20′N, 6°40′E, which is about 40 km north of the nearest station (HAU,

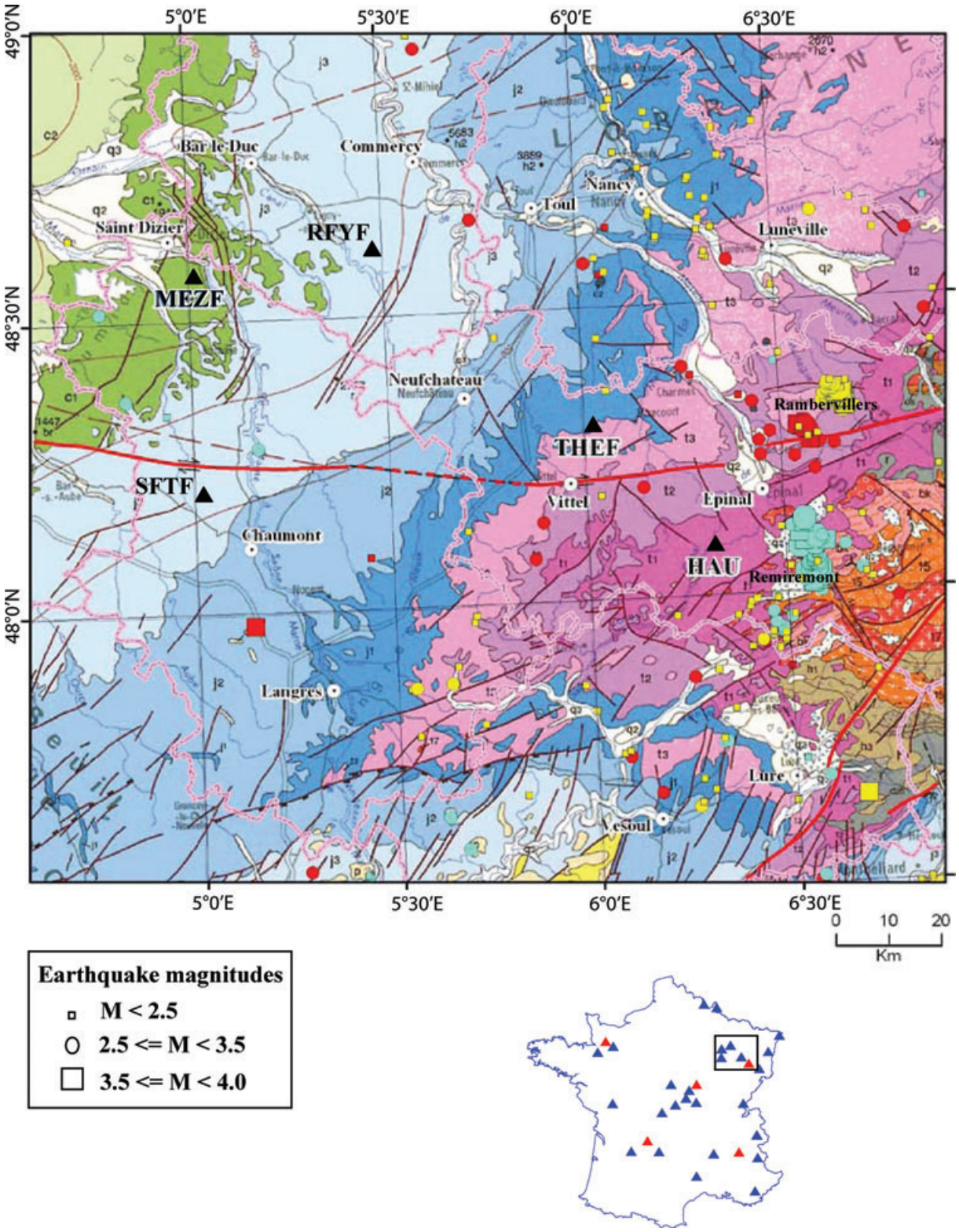

Figure 1. Simplified structural map of the western Vosges (France) showing earthquake epicentres (solid circles and squares) at the time of the Epinal (1974, red), Remiremont (1984–1985, blue) and Rambervillers (2003–2004, yellow) seismic crises. LDG-CEA seismic stations are shown as black solid triangles. c1, c2: Cretaceous; j1, j2, j3: Jurassic; t1, t2, t3: Triassic; h1, h2, h3: 'houiller' (Carboniferous); orange: Vosges granite. Sketch: LDG-CEA seismic network, showing short-period (blue triangles) and long-period (red triangles) stations.

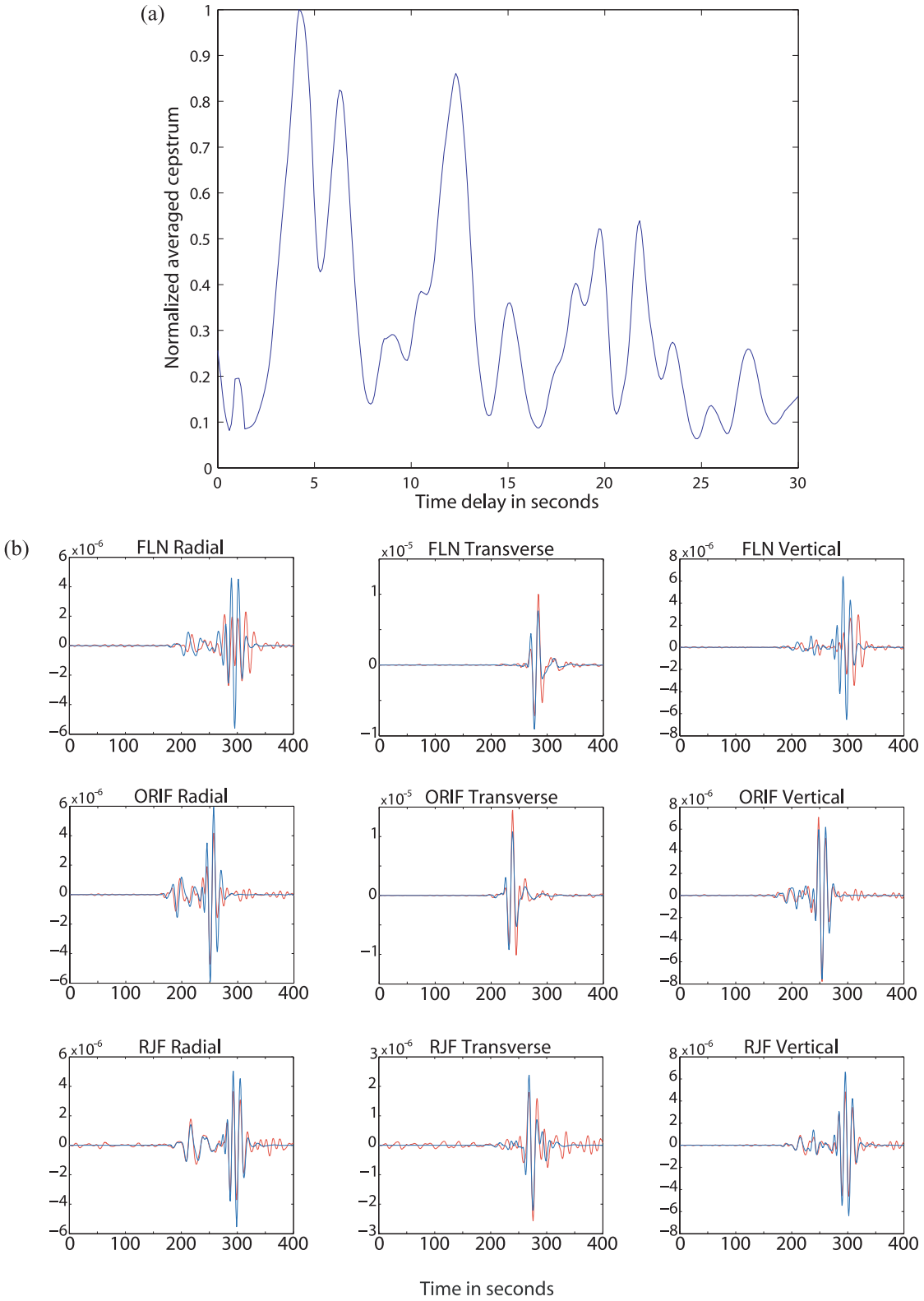

Figure 2. (a) Normalized averaged cepstrum as a function of the *pP–P* time delay. Cepstrum was averaged over the four remote dense seismic arrays used. (b) Comparison of the long-period waveforms observed at regional distance (red) with the waveforms computed using the optimal source parameters (blue). (c) Comparison of the short-period waveforms recorded by dense arrays at teleseismic distances (red) with the waveforms computed using the optimal source parameters (blue).

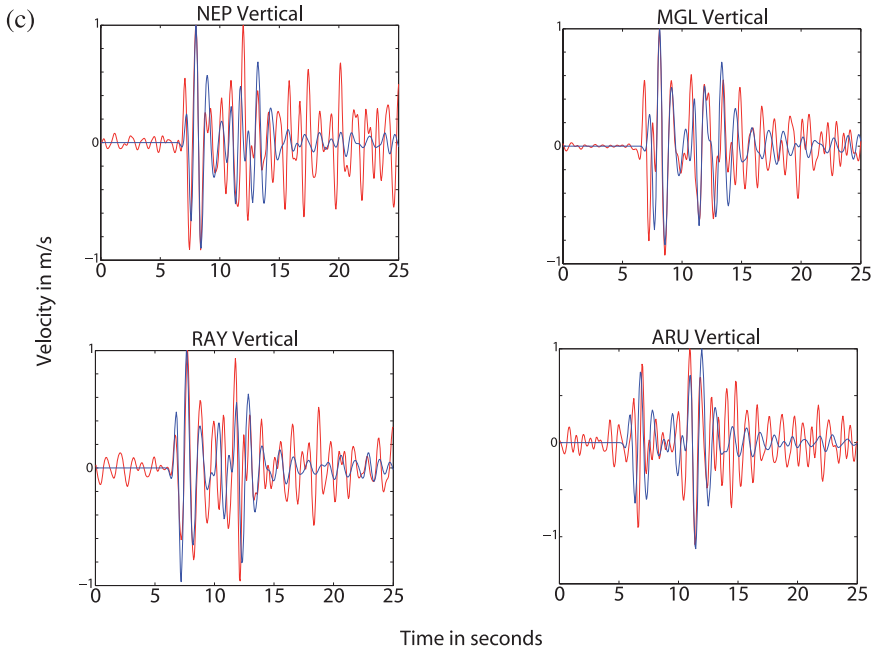

Figure 2. (*Continued.*)

Table 1. 1-D regional velocity model used for earthquake location (Plantet & Cansi 1988).

Profondeur (km)	V_p (km s^{-1})	V_s (km s^{-1})
0	3.00	1.73
0.9	6.03	3.56
25.9	8.16	4.65

Haudompre). These locations are not sufficient to give an accurate picture of the seismogenic structure. To produce a more accurate relocation, we carried out a double-difference relocation of these events, first by using their traveltime differences, and then by performing a cross-correlation of similar earthquake waveforms. To do this, we used the seismic waveforms of the earthquake sequence that occurred between 2003 February 22 and the end of 2004, and that was recorded at a 50 Hz sample rate by the permanent LDG-CEA network.

2.2.1 Preliminary location of aftershocks

To more accurately locate the largest possible number of earthquakes in the sequence, we first performed double-difference locations using traveltime differences. As there were no seismic stations very close to the earthquake swarm, the seismic network transfer function may strongly amplify the data standard deviation and induce strong location errors. When time delays are estimated from traveltime differences, rather than directly measured from waveform cross-correlation, if their distribution is Gaussian, the standard deviation of the difference will be $\sqrt{2}$ times larger than the standard deviation of the travel times. Because actual traveltime probability density functions (pdf) are long-tailed, the pdfs of their differences will have even longer tails (they are the convolution of the traveltime pdfs). Traveltime differences are not independent quantities from one event pair to another, as is the case for time delays computed from waveform cross-correlations, so the double difference process will not average the outliers. Although the modelling error tends to vanish in the differentiation of traveltimes (discarding the possibility that the solution depends systematically on the set of stations included), large outliers may occur in the data. Such outliers, even when relatively infrequent, may strongly perturbate the position of the cost function minimum. Consequently, it is necessary to take into account the actual distribution of the time difference data, at both the time difference computation step and during the inversion step.

To discard strong outliers in traveltime differences, we performed a two-step median filtering. For two events i and j of relative location vector $\mathbf{r}_{ij}$ located at the hypocentral distance Δ, when the aperture $\frac{\mathbf{r}_{ij}}{\Delta}$ is small, the time delay measured at the station k may be expressed as

$$\Delta t_{ij}^k = \mathbf{r}_{ij}\mathbf{s}^k + \Delta T_{0_{ij}}, \tag{1}$$

where $\mathbf{s}^k$ is the slowness vector at the focal depth of events i and j, and $\Delta T_{0_{ij}}$ is the correction in their origin time difference. When the wave vector set used in the relocation correctly samples the focal sphere centred on the events, $\Delta T_{0_{ij}}$ is the average of the time delays Δt_{ij}^k computed for the (i,j) event pair. To avoid perturbations due to possible strong outliers, $\Delta T_{0_{ij}}$ is best estimated using the median of Δt_{ij}^k.

By estimating $\Delta T_{0_{ij}}$, it is possible to infer the quantity $\Delta\tau_{ij}^k = \Delta t_{ij}^k - \Delta T_{0_{ij}}$, that is, the time delay due to the difference in event location. Because $\Delta\tau_{ij}^k$ is itself perturbated by outliers, the median of its absolute value provides a more robust estimator. The theoretical form of $\Delta\tau_{ij}^k$ is a cosine; therefore, the maximum geometrically acceptable value taken by $|\Delta\tau_{ij}^k|$ from its median is

$$\max\left(\left|\Delta\tau_{ij}^k\right|\right) = 2\text{median}\left(\left|\Delta\tau_{ij}^k\right|\right), \tag{2}$$

where median$(|\Delta\tau_{ij}^k|)$ is the median absolute deviation (MAD) of the time delay $\Delta\tau_{ij}^k$.

Consequently, it is possible to discard strong outliers whose values are larger than Cmedian$(|\Delta\tau_{ij}^k|)$, where C is a constant larger than 2 (typically 5). This process allows an efficient *a priori* detection of traveltime difference outliers.

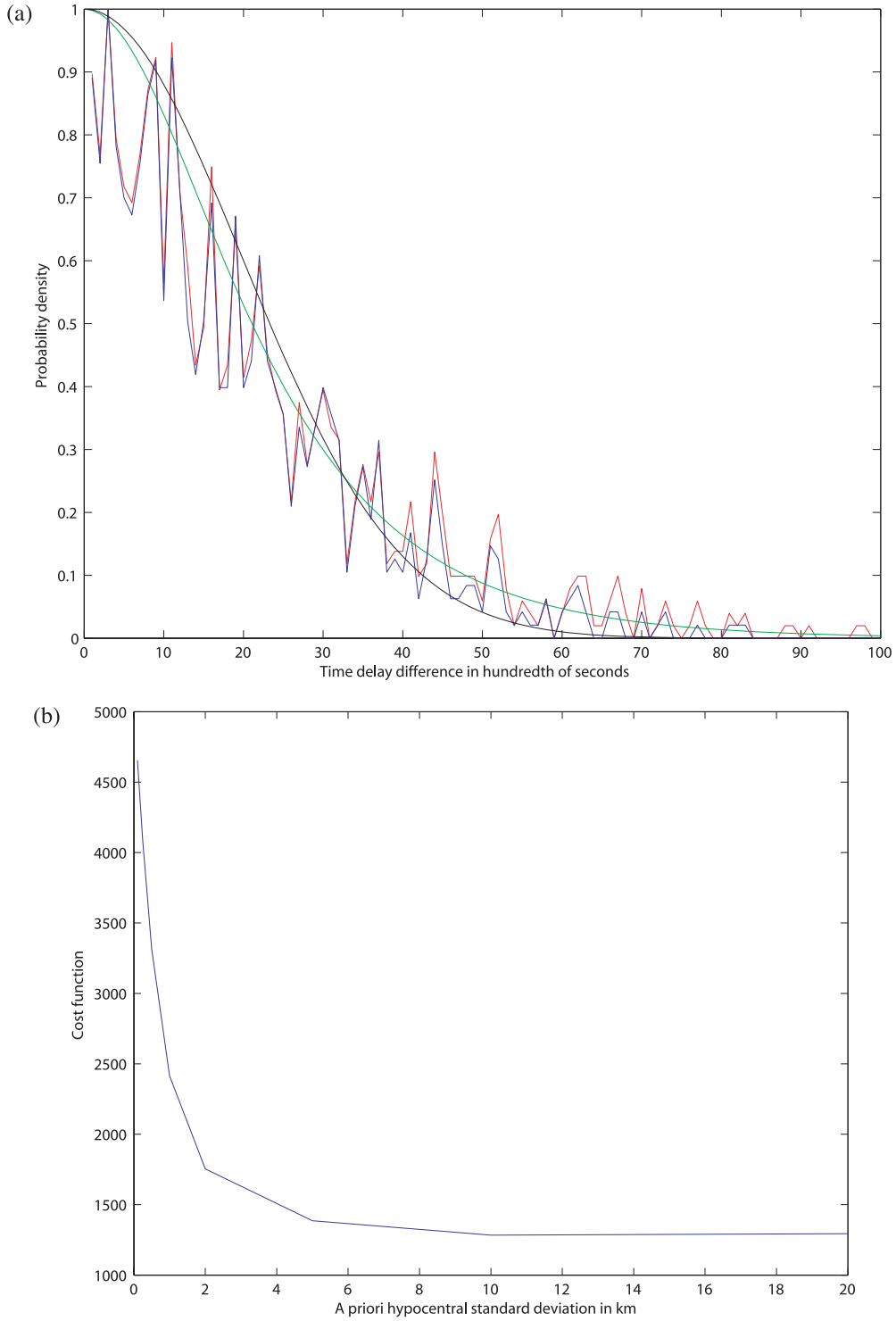

Figure 3. (a) Probability density function of the traveltime differences—red line: before outlier median filtering; blue line: after outlier median filtering. Modelling of this pdf using (i) a Gaussian function (black line) and (ii) a sech function (green line). The sech function approximately fits the pdf of the traveltime differences after median filtering. (b) Cost function and rms as a function of the *a priori* standard deviation on the hypocentral position.

Even detecting strong outliers does not imply that the distribution of time differences is Gaussian. We estimated the probability density of the traveltime difference error by computing (Section 2.2.2) the difference between the traveltime difference and the corresponding time delay difference for similar events. We modelled this probability density as a hyperbolic secant (sech) distribution rather than as a Gaussian distribution (Fig. 3a), and we fitted the traveltime distribution via a sech law with a standard deviation of 0.16 s. To take into account this distribution in the double-difference inversion process, we adopted the Bayesian approach followed by Monteiller *et al*. (2005) to locate the events. Both the data and the model parameters are considered to be affected by noise modelled as a random variable. The data follow a sech distribution and the model (hypocentral) parameters follow a Gaussian distribution.

A priori knowledge of the hypocentral parameters is given by their absolute locations and their standard deviation σ_h. As σ_h is not perfectly known, we explored wide intervals (Fig. 3b) of its value to optimize the cost function

$$(g(\mathbf{m}) - \mathbf{d})^T \mathbf{C_d^{-1}} (\mathbf{g(m)} - \mathbf{d}) + (\mathbf{m} - \mathbf{m_0})^T \mathbf{C_m^{-1}} (\mathbf{m} - \mathbf{m_0}), \quad (3)$$

where $\mathbf{m}$ is the model, $\mathbf{d}$ the data, $g(\mathbf{m})$ the theoretical travel times, $\mathbf{C}_d$ the data covariance, $\mathbf{m}_0$ the *a priori* model and $\mathbf{C}_m$ the model covariance. This approach (see Monteiller *et al*. 2005 for details) has been found to be very stable, especially when data are noisy and sparse.

From the initial set of ∼2000 events recorded during 2003–2004, we selected a set of 419 events in which each pair gave at least six non-outlier traveltime differences. We relocated these events using Plantet & Cansi's 1-D velocity model (1988; Table 1) and Monteiller *et al*.'s algorithm (2005). Optimal regularization of the inversion was found for $\sigma_h = 5$ km, which is the order of magnitude of the expected uncertainty in the *a priori* absolute locations.

The results (Figs 4a and b) show a complex, but not incoherent, space–time pattern for the distribution of the hypocentres. A striking feature is that the aftershocks immediately following the mainshock (75 events recorded by the LDG-CEA network in the first 2 days, Fig. 4c) mainly occurred on a subhorizontal plane, whereas later aftershocks mainly occurred in a confined volume dipping northward (Fig. 4b). Location uncertainties (Figs 4d and e) were calculated via an exhaustive computation of the location pdf for each of the events, which was carried out by calculating the residual standard deviation between theoretical and observed time delays in a 10 km × 10 km × 10 km volume around each event, with a 50-m sampling interval. We calculated the volumes corresponding to a 67 per cent probability (one spatial standard deviation) and determined the tangential ellipsoids (Gaussian quadratic model) by computing the eigenvalues and eigenvectors of these volumes. The horizontal uncertainty (average ∼250 m) shows that the horizontal extent of the immediate aftershocks is significant. The vertical uncertainty is larger (average ∼400 m); however, it does not fully account for the computed vertical component. Although the confidence volumes reveal the network transfer function, the characteristic dimensions of these volumes are moderate and the horizontal extents of the subhorizontal and northward dipping planes remain significant.

Other approaches can be used to illustrate the quality of the result. The internal consistency of the relative position vectors $\mathbf{r}$ with the set of traveltime differences $\Delta\tau_{ij}^k$ and the set of wave vectors $\mathbf{s}$ (s being the average slowness at the focal depth considered) may be checked using a stereogram representing the normalized time difference $\delta_{ij}^k = \frac{\Delta\tau_{ij}^k}{s r_{ij}}$ as a function of the difference between the directions of $\mathbf{k}$ and $\mathbf{r}$. This plot directly expresses the relation between the data and the model when the aperture $\frac{\mathbf{r}_{ij}}{\Delta}$ is small. In both cases (relocation of the whole set of 419 events and relocation of the 75 events in the first two days) it shows that the relative position of each pair in the cluster is generally consistent with the time difference and ray vectors, and that the average relative position error is small (Figs 5a and b). This result demonstrates that the double-difference solution is not overregularized, in that the relative positions of the events are coherent and constrained by the time difference data.

2.2.2 *Double-difference location of similar earthquakes*

The systematic identification of sets of similar earthquakes (earthquakes with similar waveforms) in a cluster requires estimates of the similarity of events. We did this by first computing the generalized coherency matrix (matrix in which each coefficient corresponds to the average coherency between the indexed events). The coherence between two signals is a function of the frequency, defined as the cross-spectrum normalized by the auto-spectra of each of the signals $x(t)$ and $y(t)$, whose Fourier transforms are $X(f)$ and $Y(f)$:

$$\tilde{C}_{xy}(f) = \frac{\overline{X(f)Y^*(f)}}{\left(\overline{X(f)X^*(f)}\right)^{\frac{1}{2}} \left(\overline{Y(f)Y^*(f)}\right)^{\frac{1}{2}}}, \quad (4)$$

where star and bar denote complex conjugation and smoothing, respectively. Each spectral quantity is smoothed over frequency, as coherence measures the linearity of the filter that exists between the two signals. Coherence, which can be viewed as the normalized Fourier transform of a tapered cross-correlation, is computed from 2.56 s signal windows, and smoothed over nine frequency samples. The signals are iteratively aligned before the final computation of the coherence. The coherency function is first averaged over frequency (3–15 Hz) to estimate the similarity between signals recorded by a given station with one coefficient. It is then averaged over stations that have an averaged coherence coefficient larger than 80 per cent, to estimate the similarity between events via a single coefficient, without pollution of that measure by the coherence computed from insignificant and noisy record pairs. The result is referred to as the averaged coherence.

We computed the averaged coherence for each possible event pair in the set of 419 events that was first located (Section 2.2.1). The average was computed for a frequency interval (3–15 Hz) and a minimum of two stations. The result of this computation (Fig. 6) shows that the distribution of the similarity is not homogeneous with time, as similar events were less numerous during the first 75 days following the mainshock than they were during the rest of the investigated time period. This feature is not related to a known change in the acquisition system, or to a change in the event recording procedure. The event set for that 75-day period has few correlations with the following events and within itself. In addition, the coherency matrix shows that similar events mostly belong to a single multiplet (set of similar events).

We used Eardley's equivalence class algorithm (Press *et al*. 1986) to extract families of similar events from the generalized coherency matrix, then we computed the cardinal for each coherency threshold in the interval [0.8, 1], in steps of 0.01. In the case of a homogeneous geometrical distribution of seismic stations and Gaussian error in time delays, increasing the multiplet cardinal decreases the average coherence and therefore the time delay accuracy, but it increases relocation accuracy as the square root of the number of time delays (Got *et al*. 1994). We therefore chose the optimal number of events to be located by minimizing a cost function chosen to represent the expected relative location error, expressed as a function of coherency:

$$\frac{1}{\sqrt{n}} \sqrt{\frac{1 - C^2(n)}{C^2(n)}}, \quad (5)$$

where C is the averaged coherence coefficient, and n is the multiplet cardinal. $\sqrt{\frac{1-C^2(n)}{C^2(n)}}$ is the standard deviation on the cross-spectrum phase, which scales the time delay error.

Plotting this cost function as a function of the multiplet cardinal n showed that it reaches a minimum (Fig. 7a). We chose to retain one suboptimal family of 195 similar events, which corresponds to a coherence threshold of 92 per cent.

Time delays were computed by the cross-spectral analysis of 2.56 s signal windows. The time delay θ is derived directly from the

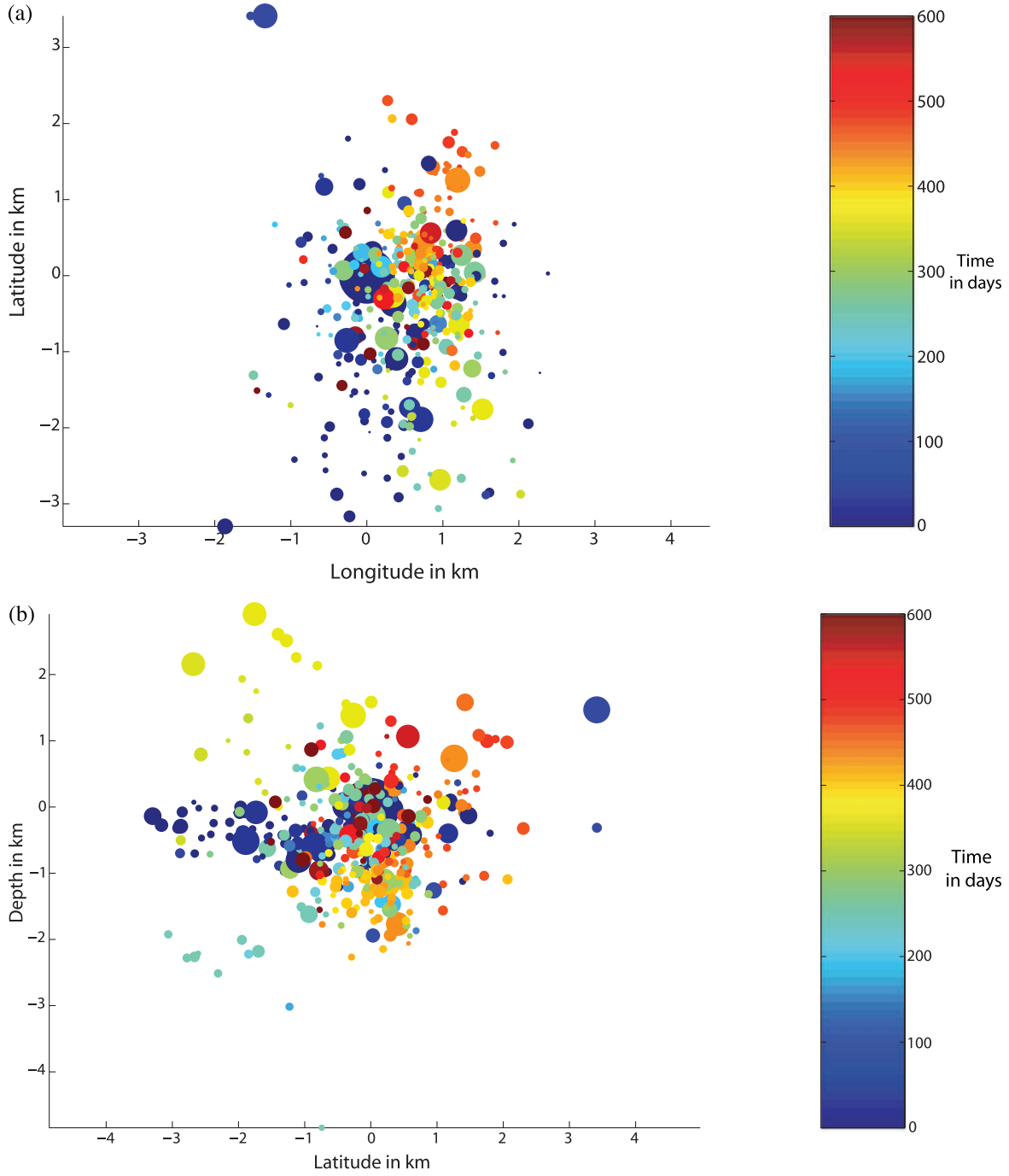

Figure 4. (a) Map and (b) NE–SW vertical cross-section of the hypocentres, showing magnitude and occurrence time of the 419 relocated events. (c) NE–SW vertical cross-section of the first 75 events, occurring during the first 2 days following the mainshock. The mainshock is shown at the origin. (d) Map and (e) NE–SW vertical cross-section of the relocated hypocentres (crosses), with their 67 per cent confidence intervals (ellipses, see text for details of the computation).

slope of the cross-spectrum phase $\phi(f)$:

$$\theta = \frac{1}{2\pi}\frac{d\phi(f)}{df}, \tag{6}$$

where f is the frequency. θ is computed by using an iterative alignment of the signals. At each step, the weighted linear adjustment of $\phi(f)$ is computed between 3 and 15 Hz, with the weight taken to be equal to the inverse of the standard deviation of $\phi(f)$. This algorithm provides the maximum-likelihood estimate of the time delay.

A first check of the quality of the time delay measurements was done by computing the closure residual error ε for the station l recording the events i, j and k:

$$\varepsilon = \frac{\Delta t^l_{ik} - \left(\Delta t^l_{ij} + \Delta t^l_{jk}\right)}{3}, \tag{7}$$

where Δt^l_{ik} stands for the time delay computed at station l between the waveforms of events i and k. Closure error is considered as uniformly distributed across the three pairs of correlated events. It was computed for every possible event triplet (i,j,k) for every

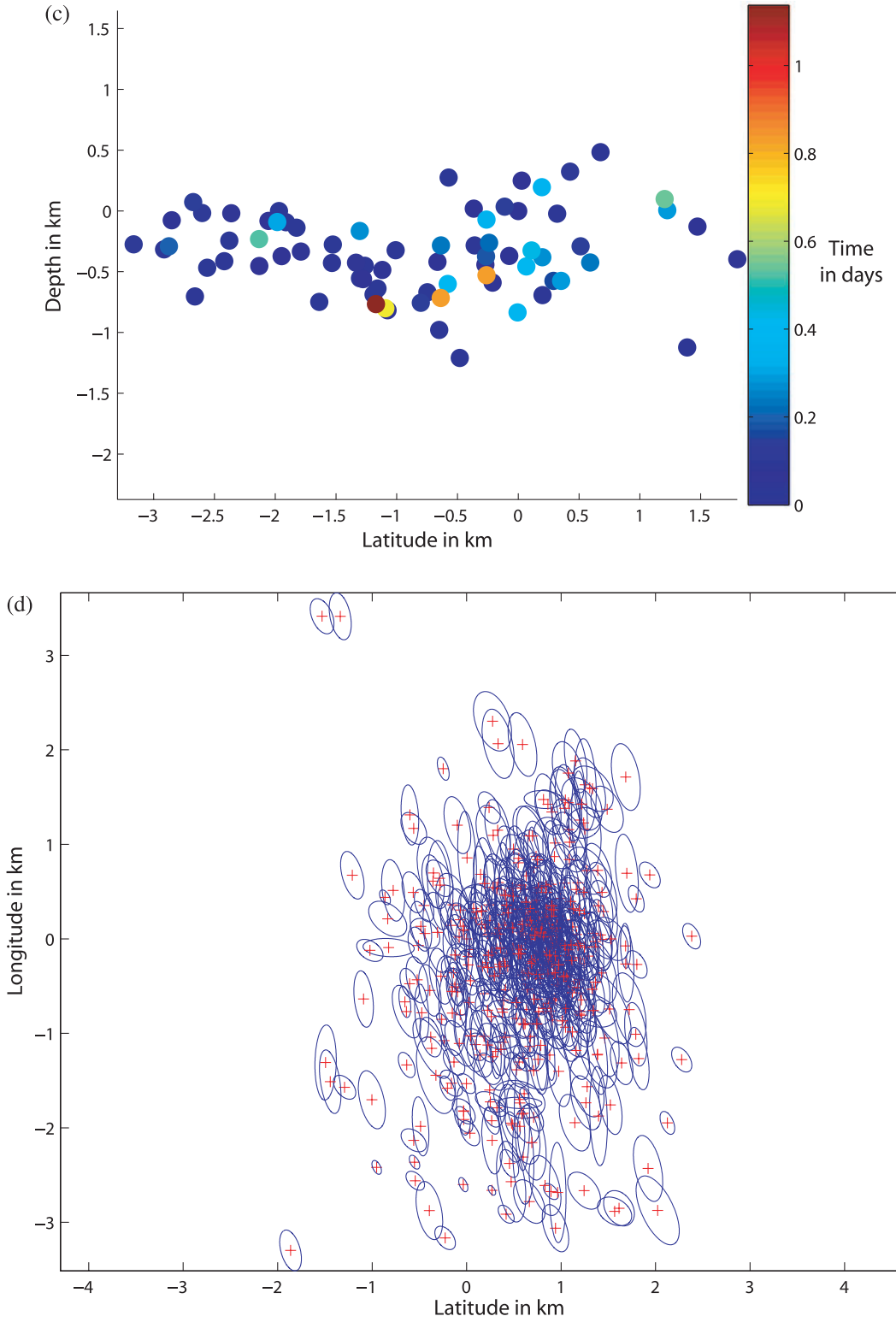

Figure 4. (*Continued.*)

recording station. The results (Fig. 7b) show that 95 per cent of the closure residual error ε is lower than 5 ms.

Time delays computed for all possible event pairs were then used to relocate similar events, which was carried out using the velocity model described by Plantet & Cansi (1988; Table 1). Because typical distances between correlated events were some hundreds of metres, and because hypocentral distances were ∼50–100 km, the time delays cannot resolve the absolute depths of events with better accuracy than the 1 km accuracy obtained using mainshock *pP* phases or short-period waveform modelling (see Monteiller *et al.* 2005). Similar events were therefore relocated relatively using an *a priori* known absolute position (depth equal to 12 km) and a linear

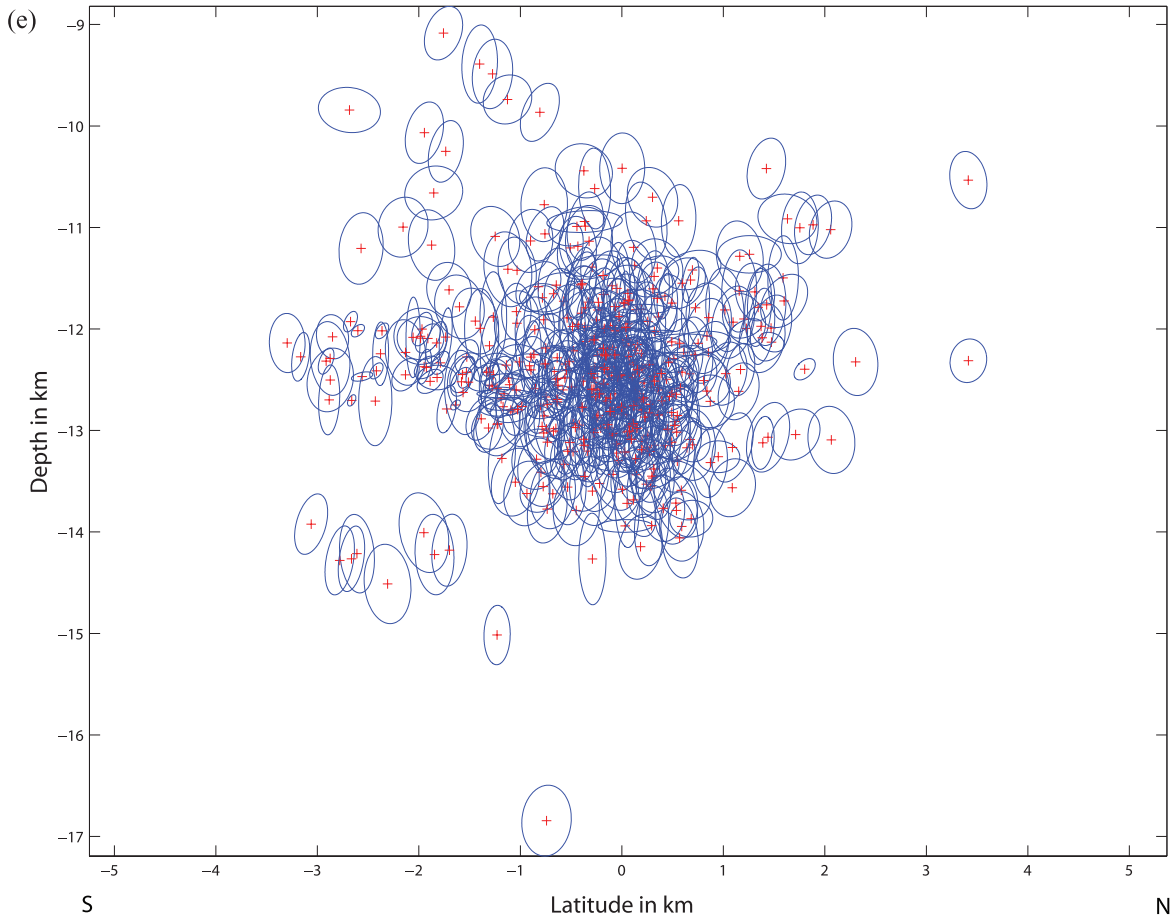

Figure 4. (*Continued.*)

double-difference relocation method (Got *et al.* 1994). Searching for relative locations led to a well-conditioned undamped inversion, and to a location RMS of 7 ms. We checked the internal consistency of data and locations (Fig. 8). Relocation revealed (Fig. 9a) an elongated NW–SE pattern for the relocated cluster (195 events), which dips ∼65°NE (Fig. 9b). The average thickness (perpendicular to the inferred average plane) is ∼150 m. The hypocentres occupy a 3 km vertical × 1 km horizontal band along this planar structure.

Several methods can be used to estimate relative position error (i.e. the internal deformation of the relocated cluster). We computed the pdf for each of the relocated events by calculating the residual standard deviation between the theoretical and observed time delays in a 10 km × 10 km × 10 km volume around each event, with a 10 m sampling interval. We determined the volumes corresponding to a 67 per cent probability and determined the tangential ellipsoids by computing the eigenvalues and eigenvectors of these volumes (Fig. 9). The ellipsoids are generally elongated with depth, showing that location pdf and error are controlled by the seismic network transfer function. The average relative position error is about 75 m horizontally and 200 m vertically. The time delay standard deviation is less than 5 ms, which would cause a ∼30 m isotropic location error for ideally distributed stations, including nadiral and epicentral stations. As a result, the location error is strongly amplified by the network transfer function. However, because the vertical error remains less than the vertical extent of the swarm, it does not hide its main geometric characteristics.

We checked the fault plane strike and dip by constructing a series of synthetic time delay sets, which were computed for various orientations of the relocated event set by rotating the events relative to the geometric centre of the set. Thus, we computed the residual standard deviation (rms) between the observed and synthetic time delays as a function of the fault plane strike and dip, keeping the respective dip and strike constant. The computation was carried out on large intervals, sampled using one-degree steps (Figs 10a and b), for the set of ray vectors corresponding to the well-constrained Plantet & Cansi (1988) 1-D regional velocity model (Table 1). For a given ray vector set it shows that the fault plane strike and dip are constrained with an error smaller than 10–15°.

2.2.3 *Temporal evolution of the seismicity*

Earthquake production rate after a mainshock is described as a function of time by the Omori law:

$$n(t) = \frac{K}{c+t}, \tag{8}$$

where $n(t)$ is the seismicity rate (number of earthquakes per unit of time), K is an amplitude factor and c is a time offset from the occurrence of the mainshock.

The Omori law may therefore be expressed in terms of the cumulated number of earthquakes $N(t)$:

$$N(t) = K \log(c+t). \tag{9}$$

We plotted $N(t)$ as a function of $\log(t)$ (Fig. 11a)—with t being counted in days from the mainshock—for the earthquakes of the Rambervillers sequence recorded up until the end of 2003 October

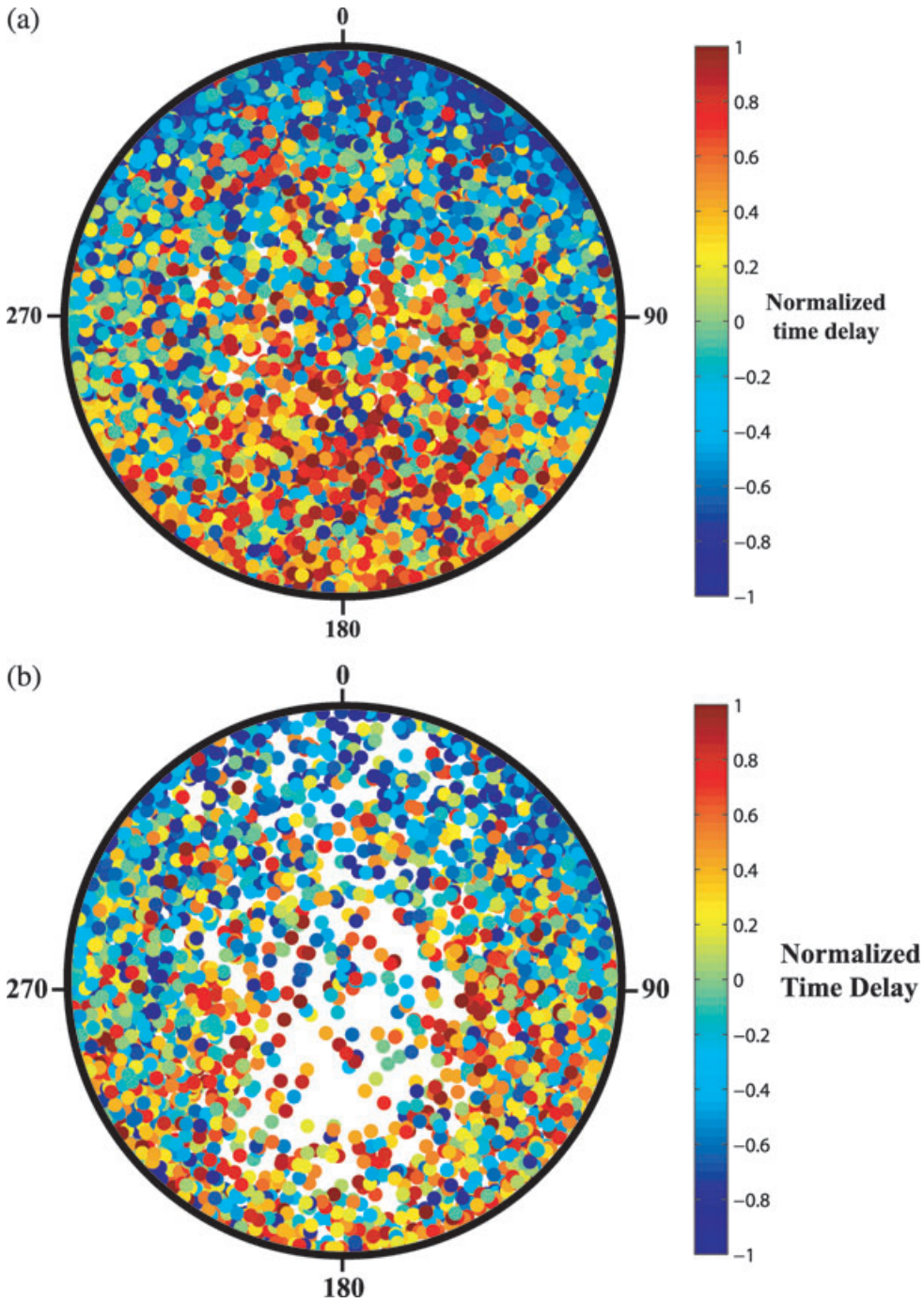

Figure 5. (a) Stereographic plot for the set of 419 relocated events (Figs 4a and b) showing the normalized time difference (see text for details) as a function of the angle (in degrees) between the relative position vector and ray direction at the focus. The set of ray (slowness) vectors is unique for the whole set of events. The time difference due to the difference in location is the dot product of the relative position vector and the slowness vector (eq. 1). A polar pattern is produced, which shows that the values of the normalized time delay are coherent with the computed relative positions. (b) Same representation for the first 75 events of the sequence, all of which occurred in the first two days following the mainshock and were located on a subhorizontal plane (Fig. 4c).

(i.e. over ∼20 months) and that were larger than the magnitude of completeness of the catalogue ($M_1 \sim 1.8$, Fig. 11b). The plot shows that $N(t)$ does not follow an Omori law for the whole time period. After $T_0 + 250$, the earthquake rate abruptly increased, indicating the beginning of a new sequence. Seven $M \sim 2.7$–3.4 (LDG) earthquakes were recorded from $T_0 + 250$ to $T_0 + 264$. More events were recorded following these seven $M \sim 2.7$–3.4 events than following the mainshock, as only 165 $M > 1.8$ events were recorded during the 250 days following the mainshock, whereas 236 events were recorded (in 200 days) following the seven 2.7–3.4 event sequence. This feature remains even when higher magnitude thresholds are used. Hence, the Rambervillers sequence was not a simple mainshock–aftershock sequence.

Plotting the occurrence time of the earthquakes as a function of their position (Fig. 12) shows that the space–time distribution of the hypocenters is not random, as a group displacement featuring

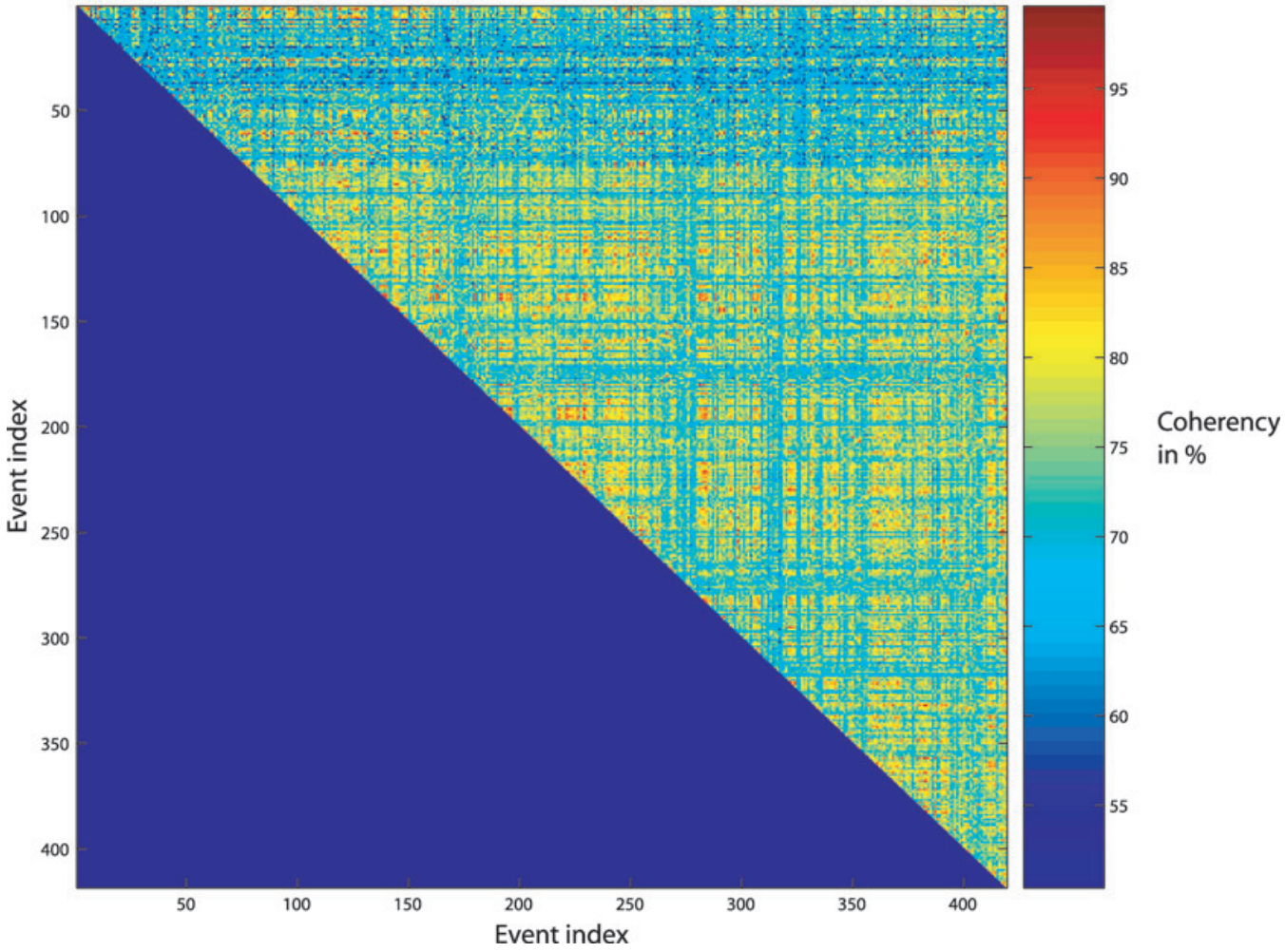

Figure 6. Generalized coherence matrix: average coherence coefficient (in per cent, colour scale) as a function of its two corresponding event indices for the set of 419 events recorded by at least six common stations.

migration over time appears. The sequence began at depth in the NW, moving up (∼2 km) after $T_0 + 200$ to the SE, and then down (∼2 km) at $\sim T_0 + 400$ to the NW. During this time period, the movement described an oscillation spanning a depth of 2–3 km, which is larger than the relative position vertical error (about 200 m). Strikingly, $T_0 + 250$ corresponds to the time when the earthquake rate abruptly changed and when the vertical movement stopped and inverted (moving up before and down after). Both the seismotectonic setting (normal faulting, i.e., local deviatoric tension, several hydrothermal sites in the western Vosges, three of them being located some tens of kilometres SW of Rambervillers) and the earthquake space–time distribution suggest a mechanism involving fluid migration.

3 DISCUSSION

Determination of the Rambervillers mainshock position using *pP* phases and short-period waveform modelling constrained its depth to 13 ± 1 and 12 ± 1 km, respectively. Long-period waveform inversion showed the mainshock focal mechanism to be a $\sim$N315° $\pm$ 10° striking, 45° $\pm$ 15° dipping normal fault plane. Double-difference location of the 419 best recorded events of the 2003–2004 Rambervillers earthquake sequence shows that most of the largest immediate aftershocks occurred on a subhorizontal plane to the south of the mainshock, whereas later seismicity developed along a more steeply northward dipping fault surface, below the mainshock. Only a few of the 419 well-recorded events that occurred in the first 75 days following the mainshock were found to be similar events. After that time, the seismicity rate increased and many more of the recorded events were similar. Careful double-difference location of these similar events showed that they occurred along a $\sim$N310° $\pm$ 10° striking, 65° $\pm$ 15° dipping fault plane. However, it is difficult to conclude from these results whether or not the plane deduced from aftershock relocation is identical to the mainshock fault plane. Because the confidence intervals for dip and direction overlap, it is not possible to differentiate between the two planes; therefore, they may represent a single normal fault plane with an average strike of $\sim$N315° $\pm$ 10° and an average dip of $\sim$55° $\pm$ 15° located at a depth of $\sim 12.5 \pm 1.5$ km.

After the mainshock, the depth of the seismicity increased and seismicity followed an Omori law for a period of 75 days. Subsequently, the seismicity rate increased and the seismicity migrated upwards. A new sequence began at $T_0 + 250$, with the occurrence of $M \sim 3$ events, followed by a sharp increase in the seismicity rate, and the inversion of the migration (seismicity depth increased). This pattern suggests fluid migration. To understand the conditions leading to such a striking seismicity pattern, we compared this set of observations with other results obtained in that region.

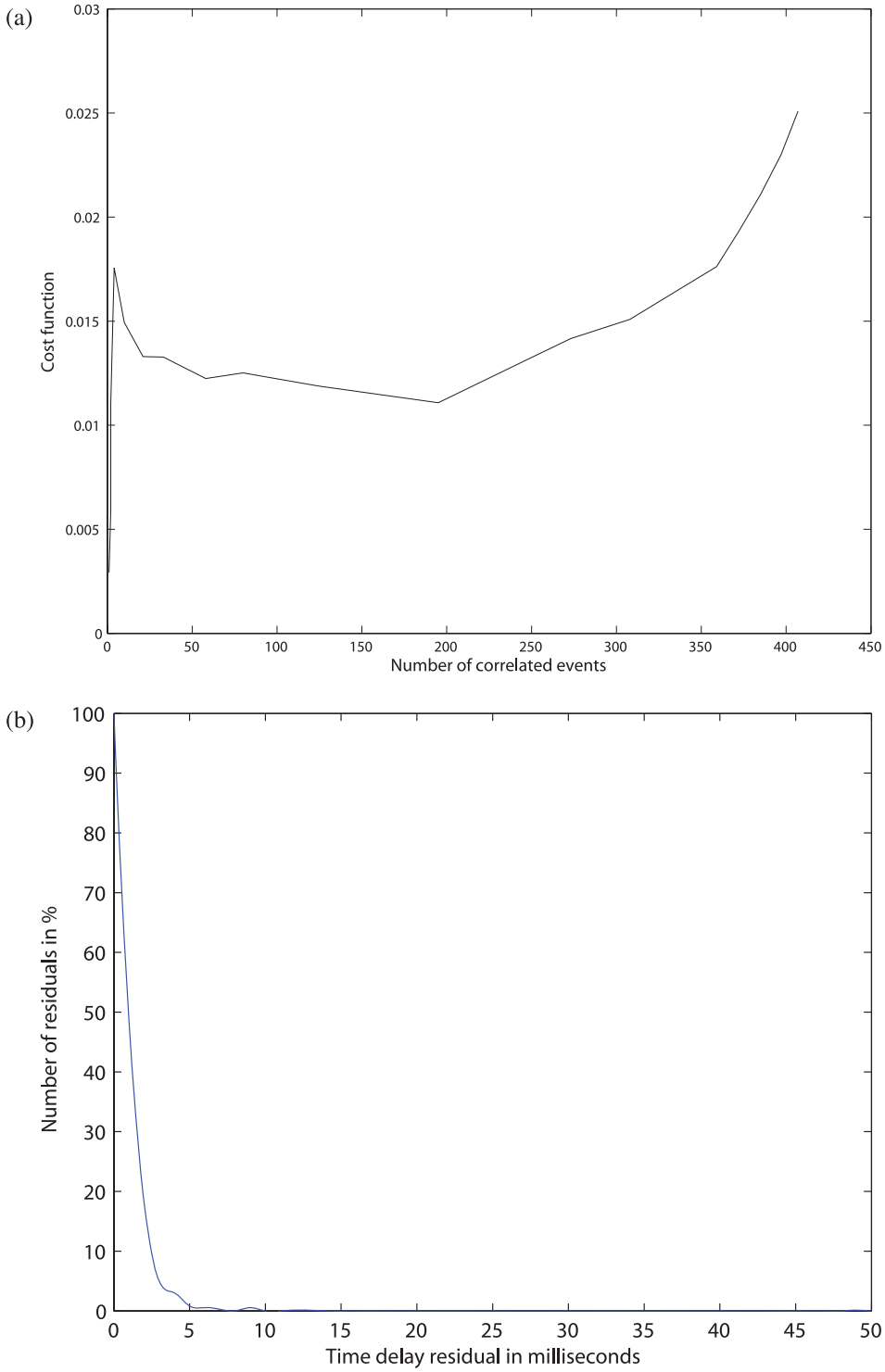

Figure 7. (a) Cost function (eq. 2) as a function of the number n of correlated events. (b) Probability density function of the closure residual error ε (eq. 7).

Understanding the horizontal development of the seismicity just after the occurrence of a steep dipping normal fault is not straightforward. Despite the care taken with the analysis, it is impossible to totally exclude earthquake effects induced by (i) magnitude filtering by the seismic network grid, (ii) the network transfer function and (iii) a lack of similarity of the recorded immediate aftershocks, all of which can conceal the aftershock activity of the mainshock fault plane. However, the vertical location uncertainty is larger than the horizontal location uncertainty and the immediate aftershocks were larger and better recorded than the subsequent aftershocks. The horizontal extent of the immediate aftershock zone is larger than the uncertainties. The vertical extent of the whole set of locations is ∼4 km. Fig. 5 shows that the time differences, ray vectors and relative positions are coherent. Therefore, the relative positions are well constrained by the data, and not overregularized by the *a priori* information ($\sigma_{\mathrm{h}} = 5$ km). The most likely explanation is that

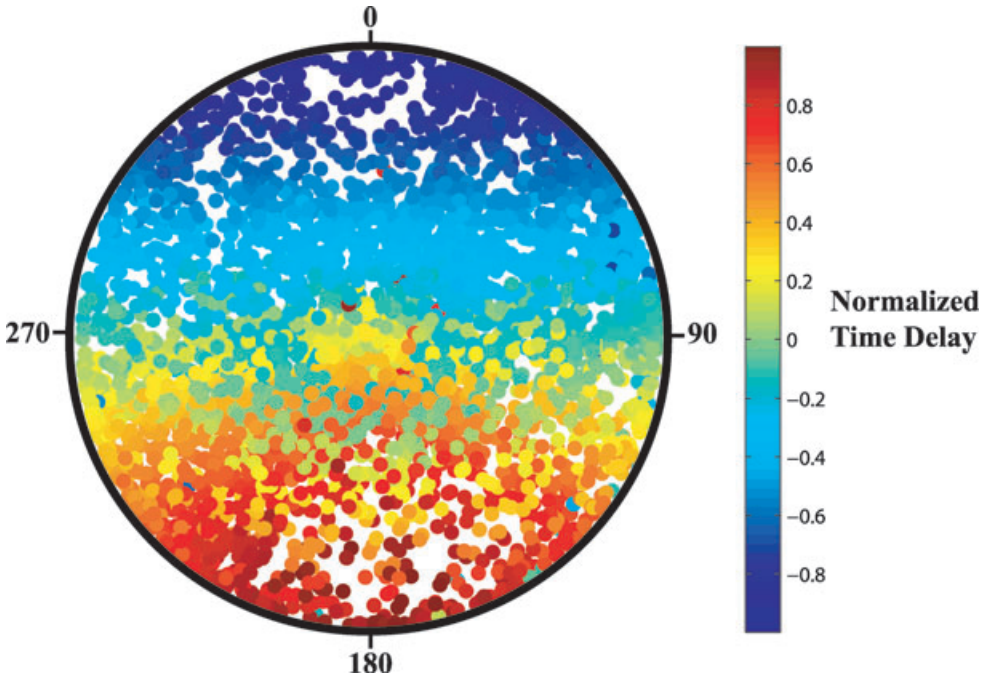

Figure 8. Stereographic plot for the set of 195 similar events showing the normalized time delay (see text and Fig. 5 for details) as a function of the angle (in degrees) between the relative position vector and the ray direction at the focus.

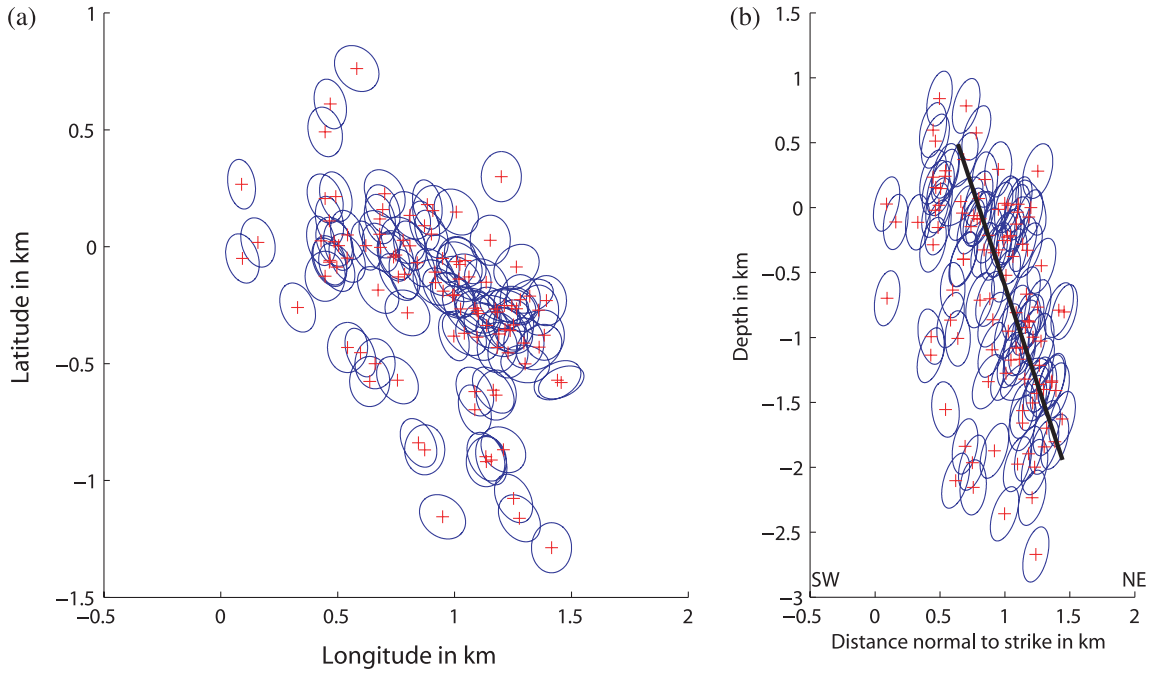

Figure 9. (a) Map and (b) NE–SW vertical cross-section of the relocated hypocentres of the 195 similar events (crosses), with their 67 per cent confidence intervals (ellipses, see text for the details of the computation). The black solid line in (b) has a 68° dip.

the magnitudes of the initial aftershocks, which occurred on the mainshock rupture plane (normal fault in a tension state of stress), were too low to be correctly recorded by the LDG-CEA network (magnitude of completeness 1.8), and were therefore not included in our catalogue. However, normal faulting and aftershocks occurring on a subhorizontal plane may have had a mechanical coherence that requires further investigation.

Microseismicity has already been described in the upper and lower crust of the Vosges and Black Forest massifs (e.g. Delouis *et al.* 1993; Plenefisch & Bonjer 1997). The stress tensor in the Black Forest, Vosges and Rhine Graben, computed from collections of earthquake focal mechanisms (see Plenefisch & Bonjer 1997), shows that the major and minor principal stresses σ_1 and σ_3 are horizontal, striking ∼N145° and N55°, respectively, in the upper crust. This stress tensor induces right-lateral strike-slip and normal components on a N315° striking, 55° dipping fault plane. In the lower crust, σ_1 is vertical but σ_3 is horizontal with a N55° strike direction (σ_1 and σ_2 permute). This stress tensor induces

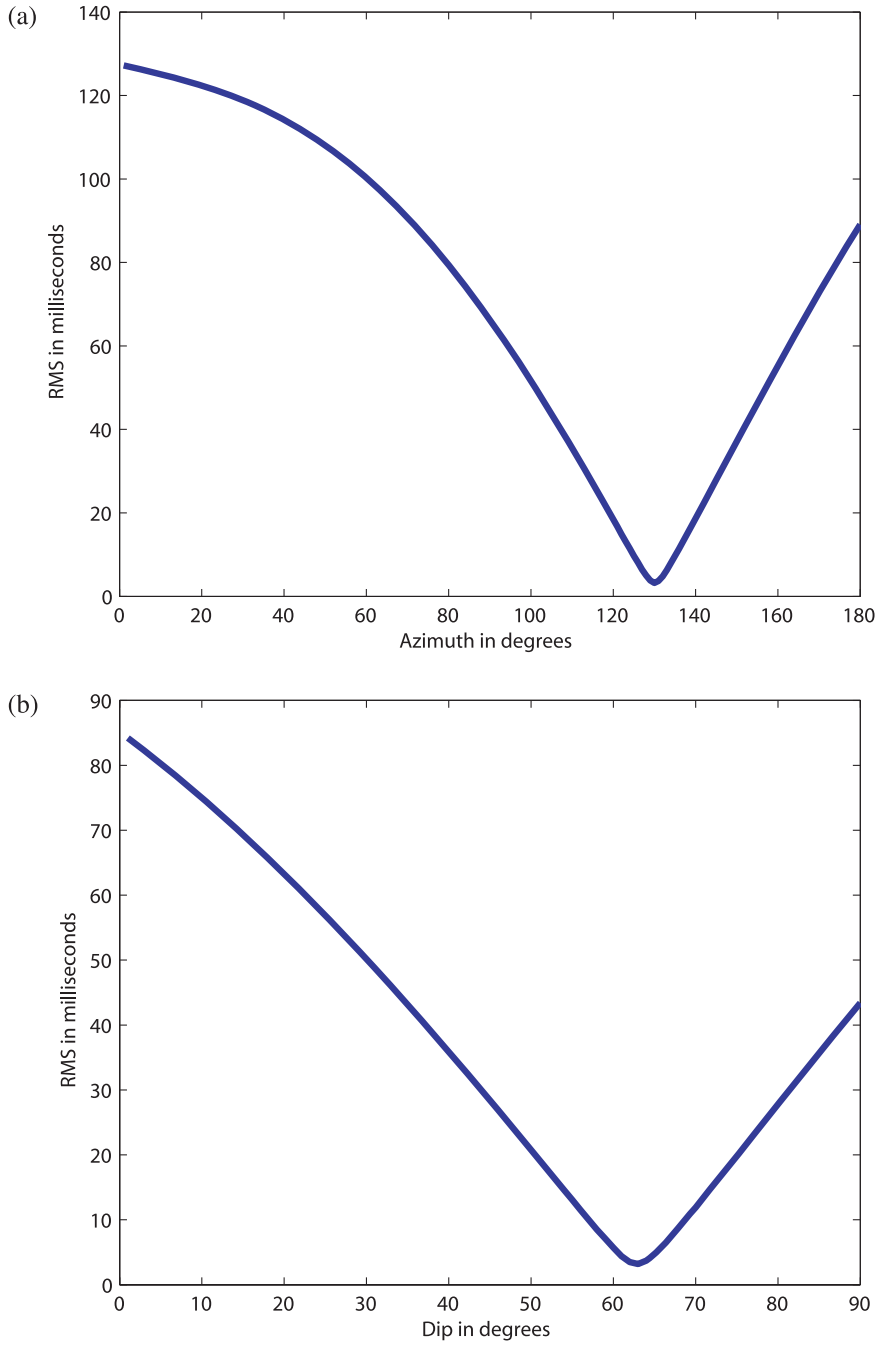

Figure 10. The rms as a function of fault plane azimuth (a) and dip angles (b), for the Plantet & Cansi (1988) 1-D regional velocity model.

normal faulting on a N315° striking, 55° dipping fault plane. The Remiremont (1984, NS left-lateral strike-slip; Haessler & Hoang-Trong 1985), Epinal (1974) and Rambervillers (2003) earthquakes (NW–SE normal right-lateral strike-slip) can be explained by the same stress tensor, which has operated since the middle of the Miocene (Villemin *et al.* 1986).

It is possible to explain the σ_1–σ_2 permutation with depth and the normal faulting at the base of the upper crust and in the lower crust in terms of the topology of the Moho in northeast France (Dèzes & Ziegler 2001; Grad *et al.* 2008; Fig. 13a). The continental crust has been flexed deeply downwards by the Alpine collision, hence, the Moho is up to 60 km deep below the Alps, but only 21–22 km deep below the Rhine Graben, where it reaches its minimum depth and forms a flexural arch. It recovers its normal depth (35 km) in NW France, under the Paris Basin. The depth of the Moho below the western Vosges is about 24 km. The continental crust between the western Vosges and the Rhine Graben is thin and has been deformed between the thicker Paris Basin and the Alpine foreland. The generally accepted depth for the brittle/ductile transition in standard continental crust (i.e. the upper/lower crust limit, see Scholz 1991) is 12 km, and this is where large intraplate earthquakes nucleate. The Moho (and continental crust) shows downward concavity below the Rhine Graben, and upward concavity in the western Vosges. In this setting, principal stress permutation may occur across the neutral surface between the upper and lower crust, at a depth of around 10–15 km. Flexural stresses may cause normal faulting in the lower

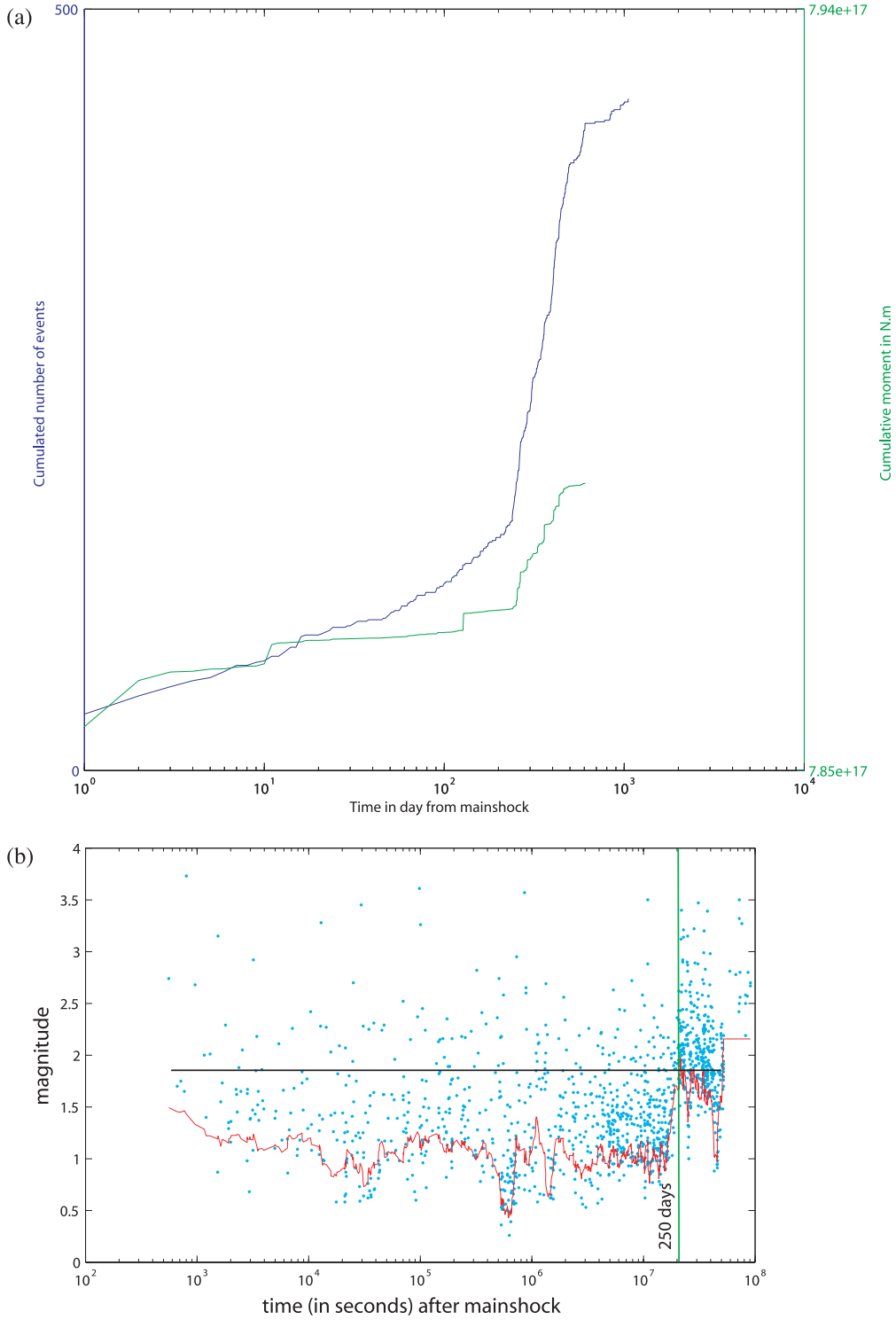

Figure 11. (a) Cumulated number and cumulative seismic moment of $M_l > 1.8$ earthquakes as a function of lapse time from mainshock occurrence, during the Rambervillers earthquake sequence. (b) Blue: magnitude of aftershocks as a function of time after the mainshock; red: magnitude of completeness computed in 20-event moving windows using Aki's (1965) estimation; black, magnitude of completeness ($M_c = 1.8$) used for (a).

crust beneath the western Vosges, whereas strike slip or even thrust faulting occurs in the upper crust. Notice that the contrast of upper crust thickness between the Vosges massif and the Paris Basin may explain the concentration of the active deformation in western Vosges. Hence, some important features of the regional stress tensor and associated strain pattern may be due to flexural stresses.

The flexuring of the crust and the upward concavity below the western Vosges with normal faulting in the lower crust is summarized in Fig. 13. Such normal faults have finite dimensions and are embedded in the crust, whose global deformation at that time is otherwise aseismic. Thus, extension in the lower crust is accompanied by contraction in the upper crust. Deviatoric stresses

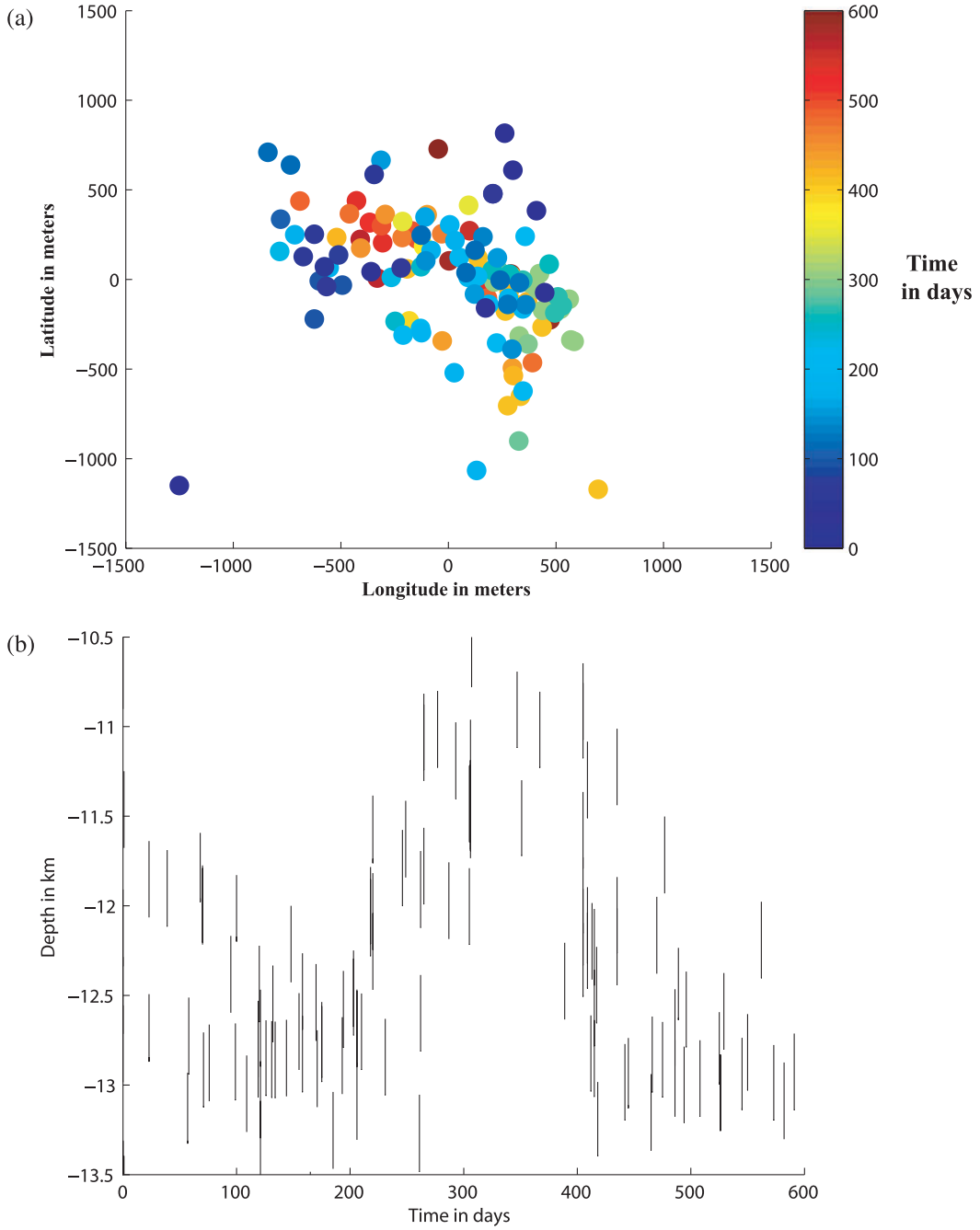

Figure 12. Occurrence time as a function of the (a) horizontal and (b) vertical positions of the relocated earthquake.

accumulate and release through subhorizontal differential displacement (readjustment), which occurs at a depth where the deviatoric stress intensity attains the rock strength. This leads to 'layer-overlayer sliding,' which may occur quasi-simultaneously with the normal fault mainshock. Accumulated elastic energy is rapidly released along the normal fault because (i) a rock's tensional strength is about 10 times lower than its compressive strength and because (ii) tension causes a loss of contact between the footwall and the hanging wall. Consequently, the residual strength of the normal fault would be expected to be weak, and its post-seismic relaxation leads to little stress accumulation and low-magnitude seismicity. In contrast, accompanying subhorizontal readjustments occur along strike-slip faults subject to a strong normal component and should induce larger magnitude aftershocks. As a result, subhorizontal aftershocks are compatible with a normal fault mainshock.

The Rambervillers seismicity occurred in several sequences. After $T_0 + 75$, the seismicity rate departed from a simple Omori law and began migrating upwards. At $T_0 + 250$, a new active sequence began migrating downwards along a 3-km-high fault plane at a depth of about 12 km. Upward migration of the seismicity was limited, although there were sufficient stresses to continue seismic deformation in another direction. In addition, Audin *et al.* (2002) showed that seismicity migrated horizontally along a ∼30 km long but vertically confined 3-km high fault zone during the 1984–1985 Remiremont earthquake sequence. Such a seismic pattern at that scale signifies a large-scale process and suggests fluid propagation

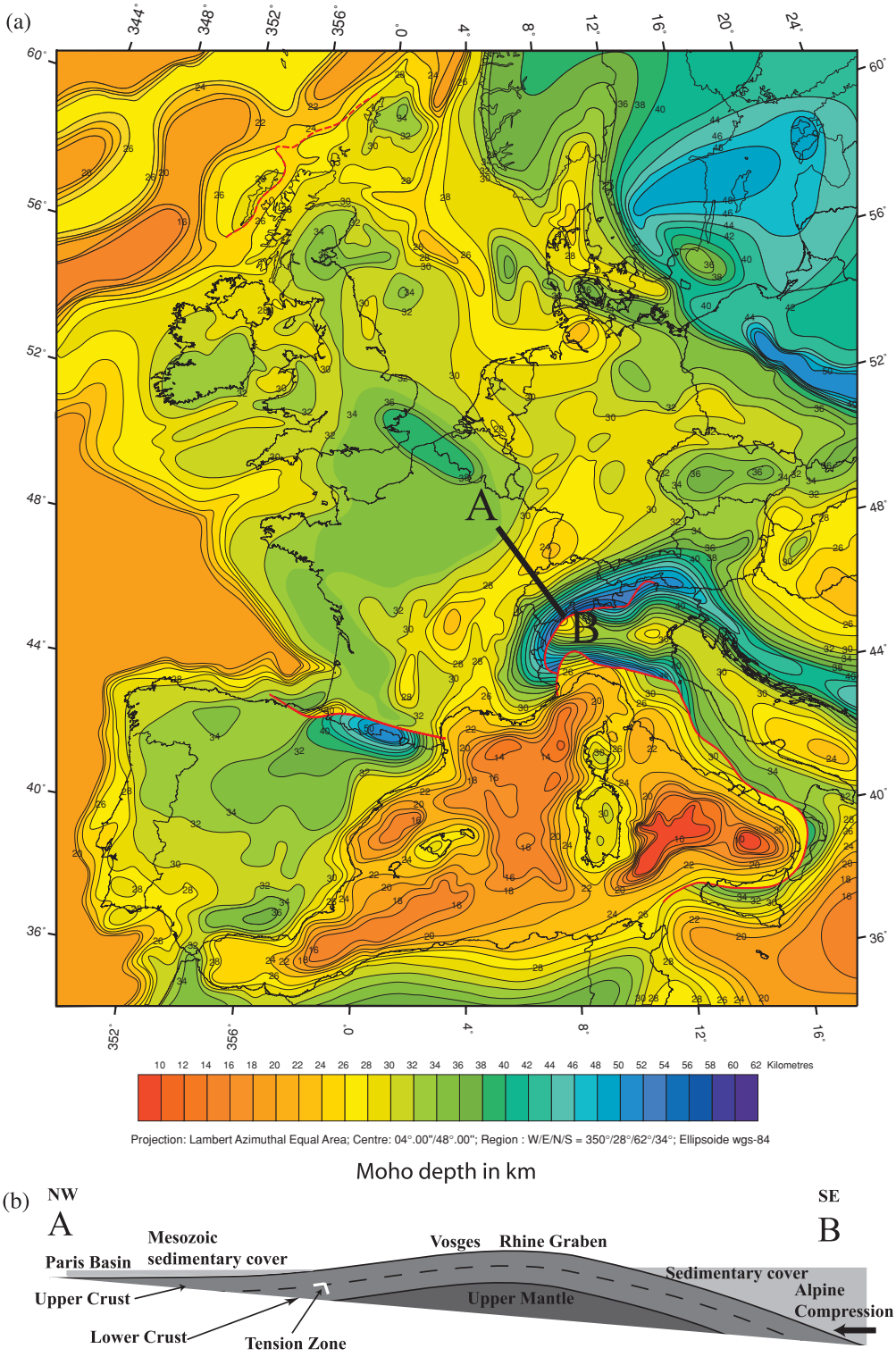

Figure 13. (a) Map of Moho depth in western Europe (from Dèzes & Ziegler 2001); bold solid line represents the direction and extent of the schematic cross-section (b). (b) Schematic SE–NW vertical cross-section showing the main features of the lithosphere in northeast France, and the position of the inferred tension zone in the western Vosges.

and confining, which may be controlled by the state of stress. This vertical confining is compatible with the local flexure and upward concavity of the crust, as horizontal deviatoric stresses are compressive above the neutral surface and tensional below it. Such a stress pattern favours the injection of pressurized fluids into the base of the lower crust and their ascent up to a limit depth in the upper crust. These fluids may propagate horizontally at the top of the tensional zone. The 12 km depth level may trap fluids and be a weak layer

that favours the development of microseismicity, despite the lack of a pre-existing fault plane. Finally, it is possible to draw up a coherent schema that may explain the spatio-temporal distribution of the seismicity in this region: due to the action of flexural stresses (induced by the alpine collision), normal faulting, and associated layer-on-layer sliding may occur. Local weakness and collapse of the crust pressurizes the fluids, leading to their (delayed) ascent to the base of the upper crust. In this interpretation, fluid transfer is evidence for post-seismic relaxation processes, invoking collapse of the crust. Is the long-term migration of the seismicity recorded during the 1984–1985 Remiremont earthquake sequence (Audin *et al.* 2002) evidence of a large-scale, progressive collapse of the crust under flexural stress conditions?

4 CONCLUSION

A detailed study of the Rambervillers earthquake sequence showed that the mainshock occurred on a N315° ± 10° striking, 45° ± 15° dipping fault plane, with a normal fault mechanism, at a depth of 12.5 ± 1 km. Double-difference relocation revealed that the largest immediate (T_0–T_{0+3}) aftershocks occurred mainly on a 5 km × 3 km subhorizontal plane. Subsequent aftershocks tended to occur on a N315° ± 10° striking, 65° ± 15° dipping fault plane, with a normal fault mechanism. Cross-spectral time delay computation using similar earthquakes was used to compute earthquake locations with an average relative vertical error (∼200 m) that was less than the vertical development (3 km) of the seismicity. These locations show that the seismicity migrated along the fault plane, migrating upward until the end of 2003 October (T_0 + 250), when several $M \sim 3$ earthquakes occurred, and then reversing to migrate downward in the subsequent seismic sequence.

This earthquake sequence may be understood in terms of the regional stress tensor (Delouis *et al.* 1993; Plenefisch & Bonjer 1997) and the topology of the Moho in northeast France (Dèzes & Ziegler 2001). The European Plate has been deeply flexed by the Alpine collision, giving it a downward concavity below the Rhine Graben and an upward concavity below the western Vosges. The stress tensor shows that contraction occurs locally in the upper crust, whereas tension occurs in the lower crust. This deformation process may induce (i) normal faulting in the lower crust, (ii) subhorizontal readjustments near the neutral surface and (iii) possible migration from depth of pressurized fluids which are then stored at the base of the upper crust. These features are compatible with the spatio-temporal distribution of the seismicity. In such settings, post-seismic relaxation may be accompanied by the weakening and collapse of the crust, fluid transfer and systematic non-Omori seismicity at the top of the lower crust.

ACKNOWLEDGMENT

This work was carried out under LDG-CEA contract #4600101825/P6H53.

REFERENCES

Abhorner, L., 1975. Present day stress field and seismotectonic block movements along major fault zones in Central Europe, *Tectonophysics,* **29,** 233–249.

Aki, K., 1965. Maximum likelihood estimate of b in the formula $\log N = a - bm$ and its confidence limits, *Bull. Earthq. Res. Inst.,* Tokyo Univ., **43,** 237–239.

Alexander, S.S., 1996. A new method for determining source depth from a single regional station, *Seism. Res. Lett.,* **67,** 63.

Audin, L., Avouac, J.-P., Flouzat, M. & Plantet, J.-L., 2002. Fluid-driven seismicity in a stable tectonic context: the Remiremont Fault Zone, Vosges, France, *Geophys. Res. Lett.,* **29,** doi: 10.1029/2001GL012988.

Bonner, J.L., Reiter, D.T. & Shumway, R.H., 2002. Application of a cepstral F statistic for improved depth estimation, *Bull. seism. Soc. Am.,* **92**(5), 1675–1693.

Bouchon, M., 1981. A simple method to calculate Green's functions for elastic layered media, *Bull. seism. Soc. Am.,* **71,** 959–1071.

Campbell, D.L., 1978. Investigation of the stress-concentration mechanism for intraplate earthquakes, *Geophys. Res. Lett.,* **5,** 477–479.

Cara, M., Brüstle, W., Gisler, M., Kästli, P., Sira, C., Weihermüller, C. & Lambert, J., 2005. Transfrontier macroseismic observations of the M_l = 5.4 earthquake of February 22, 2003 at Rambervillers, France, *J. Seism.,* **9,** 317–328.

Cotton, F. & Coutant, O., 1997. Dynamic stress variations due to shear faults in a plane layered medium, *Geophys. J. Int.,* **128,** 676–688.

Delouis, B., Haessler, H., Cisternas, A. & Rivera, L., 1993. Stress tensor determination in France and neighbouring regions, *Tectonophysics,* **221,** 413–438.

Dèzes, P. & Ziegler, P.-A., 2001. European map of the mohorovicic discontinuity, in *Proceedings of the 2nd EUCOR-URGENT Workshop (Upper Rhine Graben Evolution and Neotectonics)*, Mt. St. Odile, France.

Fischer T. & Horálek, J., 2003. Space-time distribution of earthquake swarms in the principal focal zone of the NW Bohemia/Vogtland seismoactive region: period 1985–2001, *J. Geodyn.,* **35**(1–2), 125–144.

Fischer T. & Horálek, J., 2005. Slip-generated patterns of swarm microearthquakes from West Bohemia/Vogtland (central Europe): evidence of their triggering mechanism? *J. geophys. Res.,* **110,** B05S21, doi: 10.1029/2004JB003363.

Gangopadhyay, A. & Talwani, P. 2003. Symptomatic features of intraplate earthquakes, *Seismol. Res. Lett.,* **74,** 863–883.

Got, J.-L., Fréchet, J. & Klein, F.W., 1994. Deep fault plane geometry inferred from multiplet relative relocation beneath the south flank of Kilauea, *J. geophys. Res.,* **99,** 15 375–15 386.

Grad, M., Tiira, T. & ESC Working Group, 2008. The Moho depth map of the European plate, *Geophys. J. Int.,* **176,** 279–292.

Haessler, H. & Hoang-Trong, P., 1985. La crise sismique de Remiremont (Vosges) de décembre 1984: implications tectoniques régionales, *Compte-Rendus de l'Académie des Sciences Paris*, **300**(II), 671–675.

Hinze, W.J., Braile, L.W., Keller, G.R. & Lidiak, E.G. 1988. Models for mid-continent tectonism: an update, *Rev. Geophys.,* **26,** 699–717.

Iio, Y. & Kobayashi, Y., 2002. A physical understanding of large intraplate earthquakes, *Earth Planets Space,* **54,** 1001–1004.

Kemerait, R.C. & Sutton, A.F., 1982. A multidimensional approach to seismic event depth estimation, *Geoexploration,* **20,** 113–130.

Kenner, S. & Segall, P., 2000. A mechanical model for intraplate earthquakes: application to the New Madrid seismic zone, *Science,* **289,** 2329–2332.

Kennett, B.L.N. & Engdahl, E.R., 1991. Travel times for global earthquake location and phase identification, *Geophys. J. Int.,* **105,** 429–465.

Lambert, J., 1997. Les tremblements de terre en France, BRGR, Orleans.

Liu, L. & Zoback, M.D., 1997. Lithospheric strength and intraplate seismicity in the New Madrid seismic zone, *Tectonics,* **16,** 585–595.

Monteiller, V., Got, J.-L., Virieux, J. & Okubo, P.G., 2005. An efficient algorithm for double-difference tomography and location in heterogeneous media, with an application to the Kilauea volcano, Hawaii, *J. geophys. Res.,* **110,** B12306, doi: 10.1029/2004JB003466.

Plantet, J.-L. & Cansi, Y., 1988. Accurate epicenters location with a large network. Example of the 1984/1985 Remiremont sequence, in *Seismic Hazard in Mediterranean Regions,* pp. 347–358, eds Bonnin, J., Cara, M., Cisternas, A. & Fantecchi, R., Kluwer, Dordrecht.

Plenefisch, T. & Bonjer, K.-P., 1997. The stress field in the Rhine Graben area inferred from earthquake focal mechanisms and estimation of frictional parameters, *Tectonophysics,* **275,** 71–97.

Press, W.H., Teukolsky, S.A, Vetterling, V.T. & Flannery, B.P., 1986. *Numerical Recipes: The Art of Scientific Computing,* Cambridge University Press, New York, NY, 518 pp.

Prodehl, C., Mueller, S. & Haak, V., 1995. The European Cenozoic Rift System, in *Continental Rifts: Evolution, Structure, Tectonics,* Developments in Geotectonics Vol. 25, pp. 133–212, ed. Olsen, K.H., Elsevier, Amsterdam.

Scholz, C.H., 1991. *The Mechanics of Earthquakes and Faulting,* Cambridge University Press, Cambridge, 471 pp.

Shumway, R.H., 1971. On detecting a signal in N stationarily correlated noise series, *Technometrics,* **10,** 523–534.

Špicák A. & Horálek, J., 2001. Possible role of fluids in the process of earthquake swarm generation in the West Bohemia/Vogtland seismoactive region, *Tectonophysics,* **336,** 151–161.

Sykes, L.R., 1978. Intraplate seismicity, reactivation of preexisting zones of weakness, alkaline magmatism, and other tectonism postdating continental fragmentation, *Rev. Geophys. Space Phys.,* **16,** 621–688.

Villemin, T., Alvarez, F. & Angelier, J., 1986. The Rhine Graben: extension, subsidence, and shoulder uplift, *Tectonophysics,* **128,** 47–59.

Ziegler, P.A. (ed.), 1992. European Cenozoic Rift System, *Tectonophysics,* **208,** 91–111.